

Corrosion of stainless steel 316L in molten LiCl-Li₂O-Li

William Phillips, Dev Chidambaram*

Materials Science and Engineering, University of Nevada, Reno, 1664 N. Virginia St., Reno, NV, 89557 MS0388, United States



HIGHLIGHTS

- SS316L exposed to molten LiCl-Li₂O-Li undergoes intergranular attack.
- Attack rates as high as 2.9 mm/year were observed in the presence of Li⁰.
- LiCrO₂, Li₂CrO₄, and NiFe_xCr_{2-x}O₄ were seen on SS316L surfaces in absence of Li⁰.
- In the presence of Li⁰, no bulk oxide film forms to prevent further corrosion.
- A transition between electrochemical and liquid metal attack occurs based on [Li⁰].

ARTICLE INFO

Article history:

Received 7 November 2018

Accepted 5 February 2019

Available online 8 February 2019

Keywords:

Pyroprocessing

Electroreduction

SS316L

High temperature

XPS

ABSTRACT

Exposure testing of Stainless Steel 316L was performed in LiCl-Li₂O-Li solutions at 650 °C for periods of 500 and 1000 h to investigate the effect of metallic Li on corrosion of materials used to contain the LiCl-Li₂O electrolyte for the electrolytic reduction of used nuclear fuel. Melt compositions studied consisted of LiCl containing 1 or 2 wt% Li₂O and 0, 0.3, 0.6, or 1 wt% Li. Post exposure surface analysis was performed using scanning electron microscopy coupled with energy dispersive X-ray spectroscopy, Raman spectroscopy, X-ray photoelectron spectroscopy, and X-ray diffraction. Focused ion beam and mechanical cross sections of the samples and gravimetric analyses were performed to determine the time-averaged corrosion rate for each sample. Lithium metal induced attack rates were found to be as high as 2.91 mm/y. In the absence of solvated Li in the LiCl-Li₂O system, LiCrO₂, Li₂CrO₄, and NiFe_xCr_{2-x}O₄ were observed to be the primary corrosion products. When Li was present in the melt, the oxidized alloying elements were only detectable via X-ray photoelectron spectroscopy, and the surface was primarily comprised of bare metal.

© 2019 Elsevier B.V. All rights reserved.

1. Introduction

Reduction of used oxide-based nuclear fuel is a necessary step for the incorporation of the large stockpile of used fuel from light water reactors into a pyrometallurgical-based fuel cycle [1–3]. The electrolytic oxide reduction operation developed by Argonne National Laboratory is the preferred method for the reduction of used nuclear fuel (UNF) and has been the subject of continued development [1,4–12]. In this process, declad, crushed, and pelletized UNF is placed in a stainless steel basket and cathodically polarized versus a suitable anode at a potential sufficient to reduce the oxides present at the cathode [12]. Li₂O is added in concentrations of 1–2 wt% to provide an

initial source of O²⁻ ions, which are then oxidized at the anode to form oxygen gas. The concentration of Li₂O must be carefully controlled, as the reduction of the lanthanides and minor actinides becomes thermodynamically unfavorable at high O²⁻ activities, and the anodic dissolution of Pt becomes problematic at low O²⁻ activities [11,13–15]. As the reduction proceeds, the actinide and lanthanide oxides are reduced to metallic form, while the salt soluble fission products (i.e. Cs, Sr, I, Br, etc.) form salts and dissolve into the electrolyte. Due to the close reduction potentials of Li₂O and UO₂ of –2.40 V and –2.47 V vs. O²⁻|O₂, respectively, and the necessity of applying a high overpotential to achieve a high reduction yield, metallic Li is generated at the cathode [2,12,16,17].

The Li generated at the cathode acts as an additional reduction pathway for UO₂ through direct chemical means; however, due to the solubility of Li in LiCl, some of the metallic Li dissolves into the electrolyte [15,16,18–23]. Dissolution of Li into LiCl has been noted

* Corresponding author.

E-mail address: dcc@unr.edu (D. Chidambaram).

by a number of researchers, and causes a number of changes in physical, electrical, and chemical properties of the electrolyte, as well as causing current inefficiency [16]. The exact solubility limit of Li in LiCl has proven to be experimentally difficult to determine [18,19,24]. A number of different dissolution mechanisms have been proposed by other researchers, but a consensus has yet to be reached within the community. The f-center model proposed by Bredig, et Al. treats the excess electron from solvated Li^0 as an anion vacancy, with the electron delocalized from any individual Li^+ ion core [18,25]. In this model, the solution behaves somewhat similarly to a liquid metal, with free electrons contributing to increased electrical conductivity. This model has successfully predicted the increase in solution conductivity for other alkali halide – alkali metal systems, however, the solution conductivity of the LiCl-Li system is anomalous in that it does not increase at the rate predicted by the f-center model [16,18]. Previous work in our laboratory using *in-situ* Raman spectroscopy has provided evidence of the presence of Li_g nanoclusters in solution as a colloidal suspension [26]. If Li_g clusters are present in the LiCl-Li system, they would act to keep the valence electrons of the Li_g cluster localized, thus reducing the rate of electrical conductivity increase associated with the progressive addition of Li^0 to LiCl. As the clusters would be present as a colloid, the solubility of Li^0 in LiCl would be dependent on the specific experimental parameters, leading to the variation in the measured values for solubility reported by other researchers [26].

Regardless of the molecular interactions at place within the LiCl-Li system, understanding of the effect the solution chemistry has on materials exposed to the molten LiCl-Li₂O-Li system is important for the safe and economical design of vessels and other components for use during the electrolytic reduction of used nuclear fuel. Corrosion in LiCl-Li₂O under oxidizing conditions has been widely investigated [27–34]. The most successful model of corrosion in this system is based on the Lux-Flood model of salt basicity where the rate of material degradation is dependent upon the activity of the O^{2-} anion [27,35,36]. In addition to O^{2-} activity, corrosion in molten salts is also governed by the inclusion of impurities in the melt, such as moisture or metal chlorides [35]. While the literature concerning corrosion in chloride salts is rich in diversity and discussion of corrosion mechanisms, very few studies have investigated the effect of solvated lithium metal in lithium chloride [37–44]. The studies that have been reported have been mainly of short-term duration and have been conducted under widely varying experimental parameters. Consequently, these studies conflict in their analysis on the effect of Li^0 on the corrosion of various materials in the molten LiCl-Li₂O-Li system.

Previous work in our laboratory has attempted to elucidate the effect of Li^0 and Li₂O on the corrosion of Stainless Steel 316L (SS316L), Inconel 625, and Monel 400 by parametrically varying the concentrations of Li₂O, Li, and impurity H₂O independently [41,42,44]. These studies showed that material degradation depends on the concentration of H₂O, Li₂O and Li, and that a transition from corrosion based primarily on the O^{2-} activity in the melt at low Li^0 concentrations to corrosion more similar to liquid metal attack occurs at high Li^0 concentrations. However, the short-term nature of these exposure tests necessitated the continuation of this work to verify our previous findings. In this light, the current study focuses on the corrosion of SS316L over extended time periods when exposed to LiCl containing Li₂O and Li at various concentrations. This paper presents the information gathered from SEM-EDS of the sample surfaces and cross sections, as well as XRD, XPS, and Raman spectroscopy of the surfaces to elucidate the mechanisms responsible for material degradation.

2. Materials and methods

All experiments were performed in a Vacuum Atmospheres OMNI-LAB glovebox under an Ar atmosphere containing less than 2 ppm O₂ and less than 1 ppm H₂O. Anhydrous LiCl and Li₂O were obtained from Alfa-Aesar and were of 99% and 99.5% purity, respectively. Li metal of 99% purity was purchased from Strem Chemicals. 99% purity Ni crucibles were obtained from Alfa-Aesar. SS316L coupons were cut from a 3.048 mm plate obtained from McMaster-Carr, with the certified composition given in Table 1.

The salt compositions studied consisted of LiCl containing 1 and 2 wt% Li₂O and 0, 0.3, 0.6, and 1 wt% Li, with exposure periods of 500 and 1000 h. Total salt mass contained in each crucible was 50 g. Duplicate samples were exposed for each data point, and 500 h and 1000 h exposures were conducted in parallel, with the 500 h samples removed from the experiment upon completion of the allotted exposure period. The furnace configuration used for this study is shown in Fig. 1. A 6.5 inch inner diameter, 6 inch tall cylindrical heater from Watlow (1500 W) was used to maintain a temperature of $650 \pm 5^\circ\text{C}$ for the duration of the exposure period. A 6 inch diameter graphite block was machined to accommodate 5 Ni crucibles, with slots machined to accommodate the sample hanging rods. This configuration allowed for repeatable placement of the samples within the melt during the salt replacement procedure outlined below. Two identical furnaces were constructed to maximize the number of experiments that could be ran in parallel. In operation, four experiments were ran simultaneously in each furnace, which allowed for an additional crucible location to be used for salt replacement purposes.

Prior to exposure, the metal samples were cut into 1.27 cm by 1.27 cm squares using a CO₂ laser. The samples were then polished to a 1 μm surface finish on both sides using a diamond abrasive and spot welded to loops of SS316L wire for suspension from the sample hanging rods, as was performed in our previous studies [41,42,44]. Sample hanging rods were made of like material to the samples, as alumina rods proved to be incapable of withstanding the highly reducing atmosphere directly over the molten solutions containing metallic Li for the duration of these experiments. The mass of each sample was recorded immediately prior to exposure using a high precision balance.

3. Experimental

Due to the evaporation of Li and Li₂O over time and the extended exposure periods of this study, the salt charge for each test was replaced once every 96 h to maintain the solution chemistry. To minimize the effects of impurity H₂O, LiCl was dried in a vacuum oven in air at 200 °C for 24 h before being transferred into the glovebox for storage [41,45]. Immediately prior to insertion in the primary furnace, a cleaned Ni crucible (99% purity, Alfa Aesar) containing the weighed amount of LiCl was dried under Ar for 2 hr in a dedicated furnace maintained at 550 °C. After insertion into the primary furnace, the LiCl was allowed 1 h to reach thermal equilibrium, after which time the required mass of Li₂O and Li were added to the molten salt. The melt was allowed to equilibrate for another hour prior to the transfer of the corrosion specimens from the old salt charge to the new salt charge. Sample transfer was accomplished through the use of specially fabricated tongs.

Table 1

Certified composition of the SS316L plate used in this study.

Fe	Cr	Ni	Mo	Mn	C
70.1	16.5	10	2	1.3	0.014

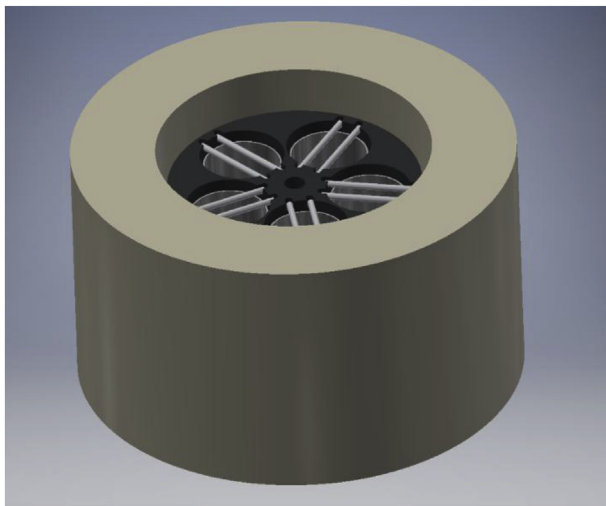


Fig. 1. A model of the long term exposure furnace, graphite crucible holder, Ni crucibles, and sample hanging rods.

Following transfer of the samples to the new salt charge, the old salt charge was removed from the furnace and allowed to cool to room temperature.

Following completion of the exposure period, the samples were removed from the furnace and allowed to cool to room temperature in the glovebox atmosphere. All samples were stored in the Ar glovebox between analytical procedures. As it was unknown if the surface films formed on the corrosion specimens would be stable in atmosphere, surface analysis was performed both prior to and following removal of the residual salt layer. Following the initial surface analytical procedures, residual LiCl was removed by placing each sample in 25 ml of HPLC grade methanol for 15 min with constant agitation. Prior to the methanol rinsing procedure, all surface analysis was performed under inert atmosphere or vacuum conditions, depending on technique. The data presented here was collected following the methanol rinsing procedure, as the residual salt layer significantly interfered with surface analysis. No chemical or morphological changes were observed as a result of the methanol rinsing procedure. Gravimetric weight change measurements were performed following the methanol rinsing procedure.

Post exposure surface analysis was performed using scanning electron microscopy (SEM) coupled with energy dispersive X-ray spectroscopy (EDS), Raman Spectroscopy, X-ray diffraction (XRD), and X-ray photoelectron spectroscopy (XPS). Following the completion of all surface analytical techniques performed in this study, the samples were cross sectioned to investigate the nature and depth of degradation of the samples. Initially, focused ion beam (FIB) milling was used to mill a trench in the samples to minimize possible morphological and chemical changes to the internal structure of the samples; however, it was found that the depth of attack for samples exposed to melts containing Li was much greater than practical to investigate using this technique alone. Consequently, all samples exposed to Li containing melts were cross sectioned using a Buehler cubic-BN wafering blade on a slow speed saw and polished according to Buehler's recommended polishing techniques to a 0.05 μm surface finish prior to analysis. Samples exposed to LiCl-Li₂O in the absence of Li were investigated using only FIB milling for cross sectional analysis due to the relatively shallow depth of attack.

SEM of the sample surfaces was performed using a Hitachi S-4700, while EDS data was collected via the attached Oxford Instruments energy dispersive X-ray spectrometer. The W cold field

emission source was operated at an accelerating voltage of 5 kV for surface morphology images, while 20 kV was used for collection of EDS spectra. Emission current was maintained at 10 mA. FIB milling and subsequent SEM-EDS analysis for cross sectional images was performed using a FEI Scios dual-beam FIB/SEM equipped with a TEAM Pegasus Integrated EDS-EBSD. The same dual-beam FIB/SEM was used to perform the SEM-EDS analysis of all of the cross sectioned samples, including those mechanically cross sectioned and polished. The electron beam was operated at 20 kV for both imaging and EDS analysis.

Following the methanol rinsing procedure, the final mass of each sample was recorded, and the exposed surface area was calculated based on the measured submersion depth of each sample. The average corrosion rate in mm/year and the mass loss rate in mg cm⁻² hr⁻¹ was then calculated based on the mass change, density of the alloy, exposed surface area, and length of exposure.

X-ray diffraction was performed using a Rigaku Smartlab X-ray diffractometer with a Cu $\text{K}\alpha$ source operating at 44 kV and 40 mA. Parallel beam optics in a grazing incidence angle configuration were used for detection of the thin surface films formed on the samples in this study. The incidence angle was set at 1°, and the diffraction pattern was recorded over a 2θ range of 10°–90° for all diffraction patterns. For each diffraction pattern, the scan speed was optimized to yield an intensity of 5000 counts for the highest peak, while the step size was varied to give 5 steps at the full width at half-maximum intensity of the narrowest peak.

Raman spectroscopy was performed using a Thermo-Scientific DXR Raman microscope utilizing a 10 mW 532 nm continuous wave laser. Spectra were collected through the 50× objective lens of the microscope using a 50 μm incident beam slit. The collection time was 4 s per spectra, and 16 individual spectra were averaged to give the spectra reported here.

X-ray photoelectron spectroscopy was performed using a PHI 5600 spectrometer equipped with an Al-K α source with a photon energy of 1486.6 eV. The source was operated at an accelerating voltage of 14 kV and an anode power of 300 W. The spectrometer dispersion and work function were calibrated to the Au 4f_{7/2} peak at 84.00 eV and the Cu 2p_{3/2} peak at 932.67 eV to an accuracy of ± 0.05 eV. Survey spectra were recorded with a step size of 0.5 eV, while narrow scans were collected at a step size of 0.025 eV for the elements detected on the sample surfaces. Peak fitting was performed with SDP version 4.6 Gaussian fitting software. Charge correction was performed to the adventitious C 1s peak at 284.8 eV unless noted otherwise.

4. Results

4.1. Scanning electron microscopy

The morphologies observed via SEM were highly dependent on the Li concentration in the molten salt solution. The SEM micrographs obtained from SS316L samples exposed to LiCl-2wt% Li₂O containing 0, 0.3, 0.6, and 1 wt% Li at 650 °C for 1000 hr and washed with methanol are shown in Fig. 2, while the area averaged EDS composition of the primary constituents of the sample surface for these regions are given in Fig. 3. The differences in the surface morphology caused by the varying concentrations of Li in LiCl-2wt% Li₂O correlates to the changes in surface chemistry observed via Raman, XPS, and XRD presented below. The unique surface morphology observed at 0.3 wt% Li may be indicative of the simultaneous action of electrochemical corrosion and liquid metal attack, while the similarity between the morphologies observed at 0.6 and 1 wt% Li indicate that corrosion at these concentrations is firmly within the liquid metal attack regime. Morphologies similar

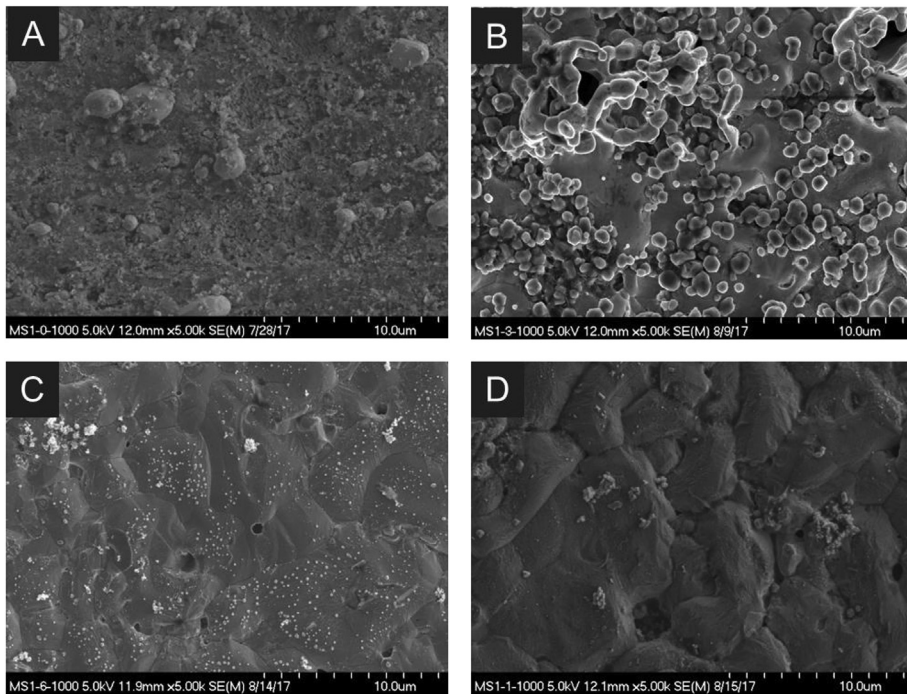


Fig. 2. SEM micrographs of SS316L exposed to LiCl-1wt% Li₂O at 650 °C containing A) no Li, B) 0.3 wt% Li, C) 0.6 wt% Li, and D) 1 wt% Li for 1000hr, following the methanol rinsing procedure.

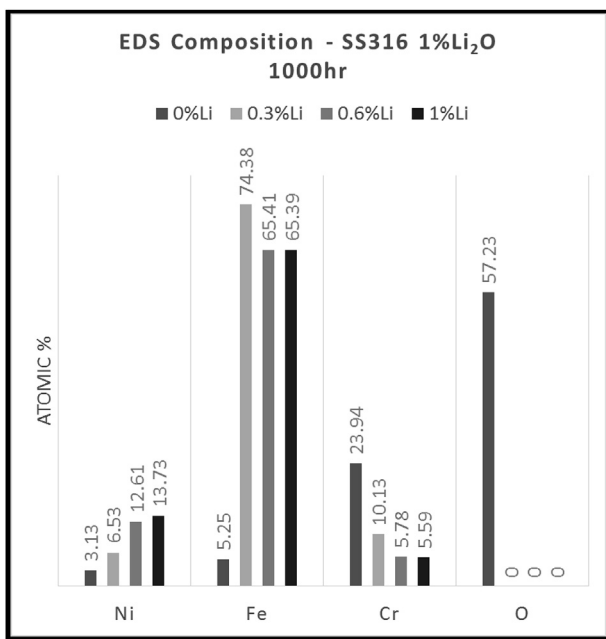


Fig. 3. Average composition of the SS316L samples exposed to LiCl-1wt% Li₂O-Li solutions for 1000hr for the regions shown in Fig. 2.

to those observed here were reported in a recent publication by researchers at KAERI who investigated the corrosion behavior of Ni in molten LiCl-Li₂O-Li [43]. A number of void spaces were also observed on the surface of all samples exposed to melts containing metallic Li, indicating possible locations where the intergranular corrosion observed on the sample cross sections was initiated. These voids were typically located at high angle grain boundaries, further supporting this hypothesis.

From Fig. 3, it can be observed that the surface of the SS316L sample exposed to LiCl-1wt% Li₂O-0wt% Li at 650 °C for 1000hr is primarily composed of Cr-based oxide films, with minor contributions of Ni and Fe. This is in good agreement with the Raman, XRD, and XPS data presented in their respective sections, which all indicate that these surfaces are composed primarily of LiCrO₂, while small quantities of Li₂CrO₄ and NiFe_xCr_{2-x}O₄ are predicted by Raman and XPS. When the Li concentration in the molten salt solution is 0.3 wt%, the Cr content of the surface is depleted compared to the base alloy while the Fe content is increased. Beyond the solubility limit of Li, at 0.6 and 1 wt% Li, Cr is depleted slightly further and O is not detectable, while both Fe and Ni are present at levels nominal for SS316L, indicating a bare metallic surface. A slight enrichment of Ni on the SS316L sample exposed to LiCl-2wt% Li₂O-1wt% Li for 1000hr is in agreement with our previous work, and is indicative of liquid metal like attack by Li [41]. Similar trends were observed for samples exposed to LiCl-Li₂O-Li containing 1 and 2 wt% Li₂O and 0, 0.3, 0.6, and 1 wt% Li for 500 and 1000hr.

Also of interest is the observation of sensitization on a small area on the SS316L sample exposed to LiCl-2wt% Li₂O-0.6 wt% Li at 650 °C for 1000hr. Sensitization of austenitic stainless steels is a well-known issue at high temperatures, where the formation of chromium carbides and their subsequent concentration at the grain boundaries leads to intergranular corrosion and loss of strength [46]. The characteristic enrichment of Cr at the grain boundaries typical of sensitization can clearly be observed in the Cr K_α EDS map in Fig. 4, while the specific compositions for spots 1 and 2 marked on the SEM micrograph and EDS map are given in Table 2.

The detection of S along with chromium carbide formation at Spot 1 is in good agreement with literature, as S is known to accelerate the sensitization of austenitic stainless steels [46]. As expected, the area around spot 1 (spot 2) has much lower concentration of chromium, which is below the concentration in base alloy. The low carbon content of the SS316L used for this study is intended to minimize this issue by preventing the formation of

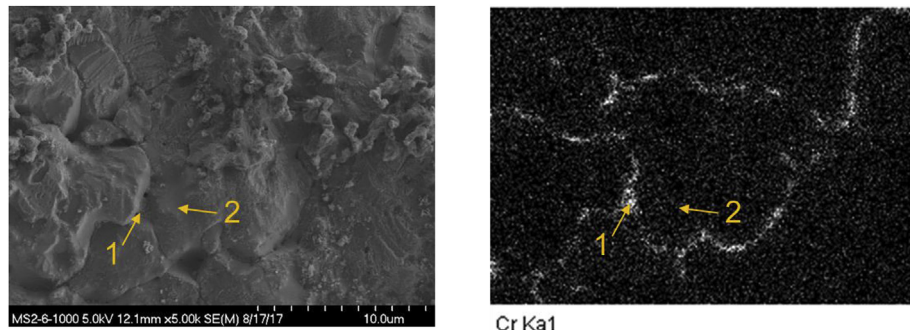


Fig. 4. SEM micrograph (left) and EDS map of Cr of the same location (right) for the SS316L sample exposed to LiCl-2wt% Li₂O-0.6 wt% Li at 650 °C for 1000hr. The elemental compositions obtained via EDS analysis for spots 1 and 2 are given in Table 2.

Table 2
EDS composition spot analysis for the locations marked on the SEM micrograph in Fig. 4, above.

Element	Spot 1	Spot 2
	Atomic%	Atomic%
C	26.69	—
S	1.21	—
Cr	27.05	4.28
Mn	1.09	1.46
Fe	28.52	50.05
Ni	15.44	44.21

carbides. Of great importance to the present work, the operating temperature of the electrolytic reduction of UNF at 650 °C is also ideal to cause sensitization of austenitic stainless steels, as chromium carbides are insoluble at this temperature and the diffusion of C through the microstructure allows for their formation and migration to the grain boundaries.

4.2. Cross section SEM-EDS

The SEM image obtained for the FIB milled trench from the SS316L samples exposed to LiCl-1wt% Li₂O-0% Li for 500hr and 1000hr are shown in Fig. 5. It can be observed that the attack first proceeds inward from the sample surface in an intergranular fashion prior to consuming the grains themselves, likely assisted by the sensitization of the material seen in Fig. 4. The depth of attack into the sample is approximately linear with length of exposure, with the total depth of attack being 13 μm and 27 μm for 500hr and 1000hr, respectively, while the thickness of the outer oxide layer is approximately 3 μm for the 500hr sample and 7.5 μm for the 1000hr sample.

EDS mapping results for the corroded region of the SS316L

sample exposed to LiCl-1wt% Li₂O for 1000hr are shown in Fig. 6. Here, it can be observed that the corrosion products (dark regions) are enriched in Cr, Mo and O, while the bulk material is relatively depleted in Cr and Mo. This agrees with the findings of previous studies that corrosion in LiCl-Li₂O occurs primarily through preferential attack of the most active alloying elements, namely Cr and Mo [35,41].

In the presence of Li, intergranular corrosion was again observed to be the primary method of material degradation, as can be observed in Fig. 7. However, the lack of a protective oxide layer severely accelerated the attack of the base material.

From Fig. 7, it can be observed that the depth of attack on the base material is approximately linear with time and does not depend on the concentration of Li; however, the severity of the degradation is proportional to the Li concentration in the melt. In all cases, the rate of attack was approximately 2.2–2.9 mm/year in the presence of Li. The outer layers of the SS316L samples exposed to melts containing Li were depleted in Cr, while small, localized areas of high Cr concentration were observed in intergranular regions, further corroborating the observations of sensitization made in Fig. 4. A high magnification EDS map of one of these regions on the SS316L sample exposed to LiCl-1wt%Li₂O-0.6 wt%Li for 500hr is shown in Fig. 8, while the spot EDS analysis for the area highlighted in red in the SEM image is given in Table 3.

From the SEM-EDS images in Fig. 8 and spot analysis in Table 3, it is apparent that corrosion of the base material is facilitated by the precipitation of Cr and Mn at the grain boundaries in the form of metal carbides and nitrides. These carbides and nitrides are then preferentially attacked by the molten salt, leaving a channel for further intrusion of the salt along the grain boundary. N was likely incorporated as an impurity from the glovebox atmosphere which reacted with Li⁰ to form Li₃N, which is known to accelerate corrosion in the LiCl-Li₂O-Li system [47]. Also, titanium nitride surface

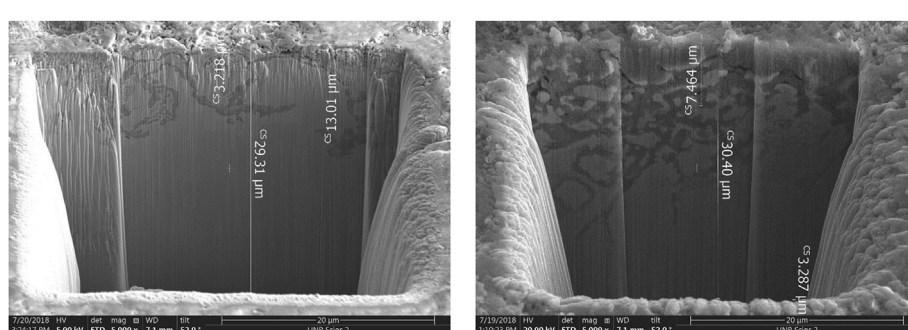


Fig. 5. FIB milled and SEM imaged cross sections of SS316L samples exposed to LiCl-1wt% Li₂O for 500hr (left) and 1000hr (right).

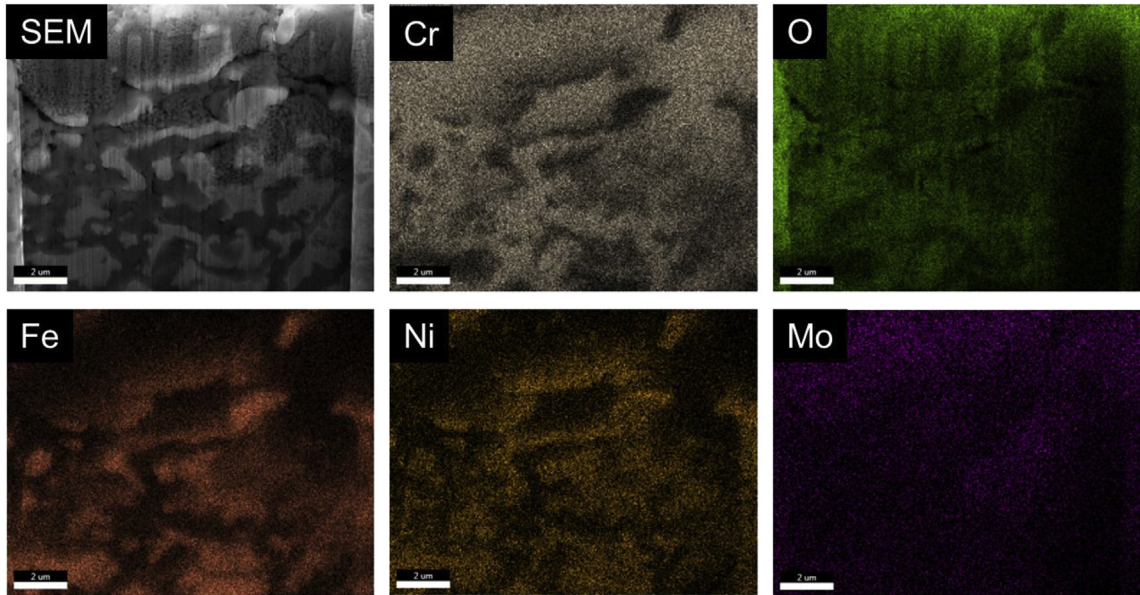


Fig. 6. EDS mapping results for the SS316L sample exposed to LiCl-1wt% Li_2O for 1000hr.

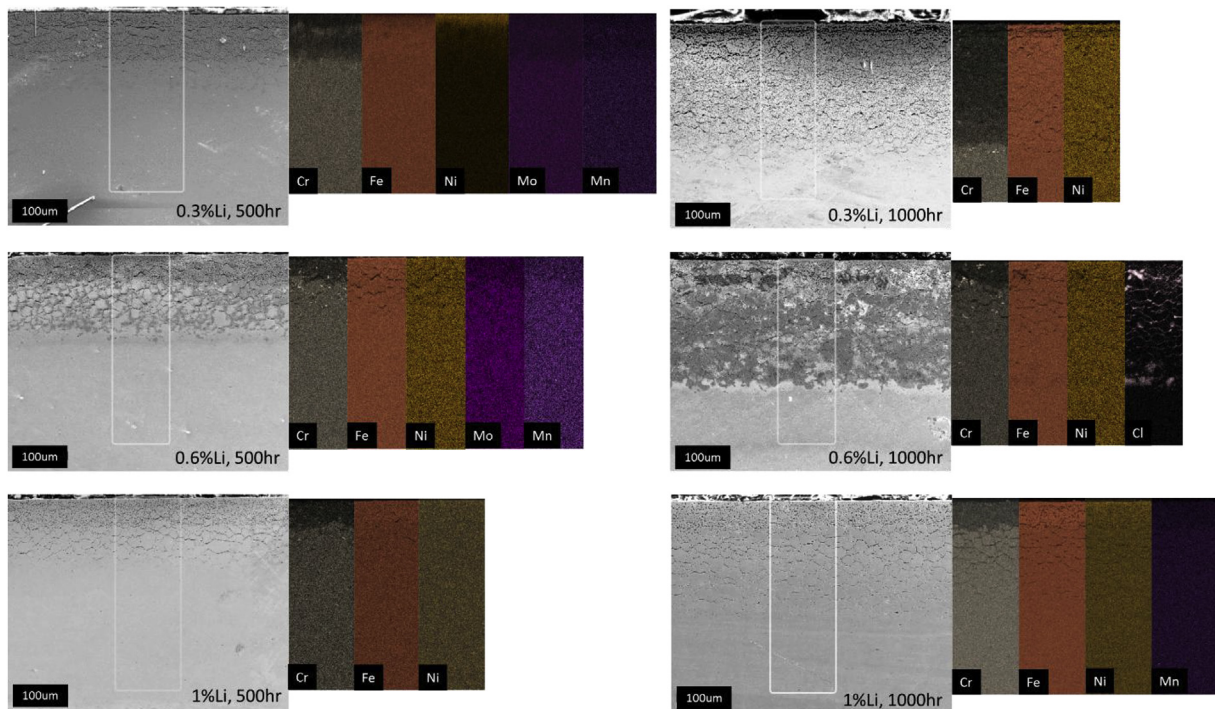


Fig. 7. Cross section SEM images and EDS maps of SS316L samples exposed to LiCl-1wt% Li_2O containing 0.3, 0.6, and 1 wt% Li for 500 and 1000hr. Areas selected for EDS mapping are delimited in SEM image. Brightness has been adjusted for clarity.

films were observed in previous studies, as well as during XPS analysis of these samples [48]. Some of these samples were observed to spontaneously form droplets of water from the cross sectioned surface when exposed to atmosphere, implying LiCl was entrapped within the sample. LiCl is extremely hygroscopic, and will absorb enough water to form a solution, even in relatively dry air, so the formation of water droplets on the cross sectioned surface is indicative of the entrapment of LiCl within the bulk sample. As most other metal chlorides are not hygroscopic to the same extent as Li, this indicates that the Cl observed in Figs. 7 and 8 is

primarily in the form of LiCl.

4.3. Depth of attack analysis

Based on the depth of attack observed in Fig. 7, the penetration rate was calculated for each sample and are tabulated in Table 4. For comparison, the corrosion rates based on gravimetric analysis are presented in Table 5.

The lack of spallation of the material based on the gravimetric analysis presented below, along with the morphological changes to

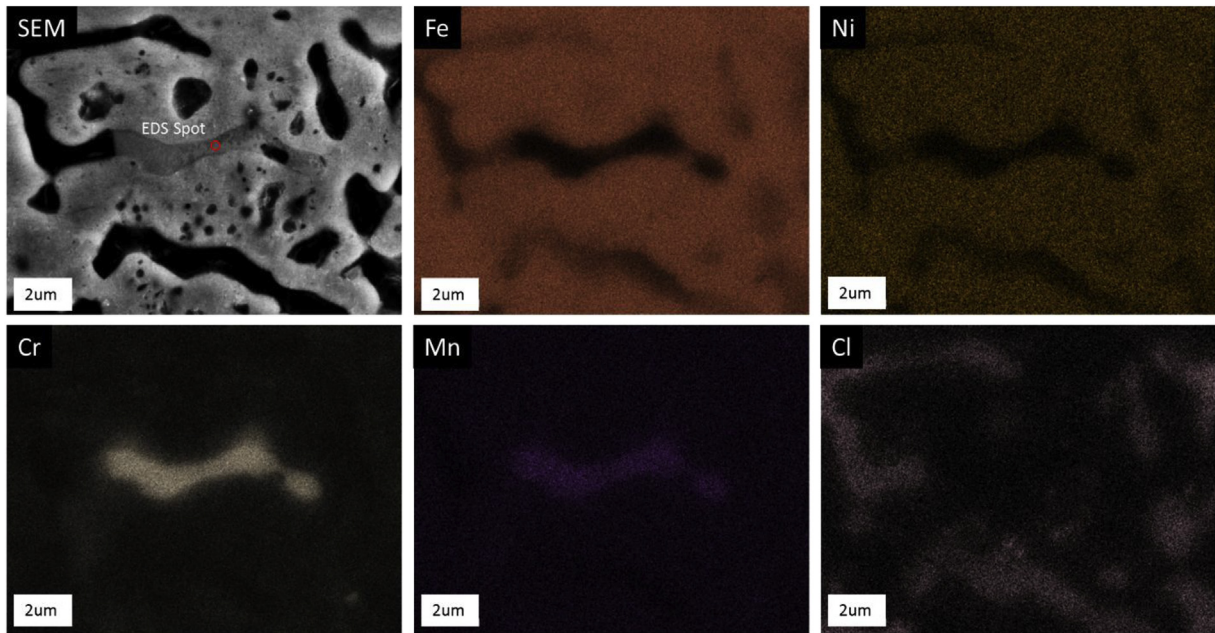


Fig. 8. Hi-magnification SEM-EDS maps of Fe, Ni, Cr, Mn, and Cl for a Cr rich region of the SS316L sample exposed to LiCl-1wt%Li₂O-0.6 wt%Li for 500hr. The red spot on the SEM image indicates the location of the spot EDS analysis summarized in Table 3. (For interpretation of the references to colour in this figure legend, the reader is referred to the Web version of this article.)

Table 3

Spot EDS analysis for the location on the SS316L sample exposed to LiCl-1wt%Li₂O-0.6wt%Li for 500hr shown in Fig. 8.

Element	Weight %	Atomic %	Error %
C	9.72	26.31	8.88
N	10.88	25.23	8.87
Cr	53.57	33.48	1.64
Mn	1.36	0.81	7.84
Fe	21.91	12.75	2.74
Ni	2.56	1.42	5.82

Table 4

Depth of attack observed for SS316L samples exposed to LiCl-1wt% Li₂O solutions containing 0, 0.3, 0.6, and 1 wt% Li for 500 and 1000hr, and the penetration rate based on this depth of attack.

Li Concentration in Salt (wt%)	Exposure Duration (hr)	Depth of Attack (μm)	Penetration Rate (mm year^{-1})
0	500	13	0.23
0	1000	27	0.24
0.3	500	140	2.45
0.3	1000	275	2.41
0.6	500	166	2.91
0.6	1000	250	2.19
1	500	120	2.10
1	1000	225	1.97

the base material shown above indicates that simple mass loss or thickness measurements are not sufficient for assessing corrosion damage in this system. The maximum corrosion rate observed gravimetrically was for the SS316L sample exposed to LiCl-1wt% Li₂O-1wt% Li for 500hr, where the corrosion rate was 0.665 mm/year, which is well below the attack rate calculated for this sample based on the ingress of attack observed in cross sectional imaging. The high variance observed is thought to be a result of the relatively low absolute weight change per sample, which was on the order of 10s of mg for most samples, as well as ingress of salt into the

Table 5

Calculated corrosion rates for SS316L samples exposed to LiCl-Li₂O-Li solutions at 650 °C for 500hr and 1000hr. Positive corrosion rates indicate weight loss, while negative corrosion rates indicate weight gain.

Wt% Li ₂ O	Wt% Li	Exposure (hr)	Mass Loss Rate ($\text{mg cm}^{-2} \text{hr}^{-1}$)	Corrosion Rate (mm year^{-1})
1	0	500	0.000	-0.005
1	0.3	500	-0.019	0.211
1	0.6	500	-0.012	0.126
1	1	500	-0.061	0.665
2	0	500	-0.010	0.115
2	0.3	500	-0.005	0.055
2	0.6	500	-0.001	0.016
2	1	500	0.012	-0.134
1	0	1000	-0.005	0.050
1	0.3	1000	-0.006	0.062
1	0.6	1000	-0.016	0.179
1	1	1000	-0.010	0.112
2	0	1000	-0.008	0.082
2	0.3	1000	-0.012	0.130
2	0.6	1000	-0.009	0.101
2	1	1000	-0.007	0.073

material. No overall trend in gravimetric weight loss as a function of material, Li₂O concentration, Li concentration, or exposure period was observed.

4.4. X-ray diffraction

Fig. 9 shows the diffraction pattern obtained for SS316L exposed to LiCl-2wt%Li₂O-0wt%Li at 650 °C for 500hr. Peaks characteristic of LiCrO₂, based on PDF card number 01-072-7839, and the base material were observed [49]. No other phases were detected on the sample surface, indicating that the NiFe_xCr_{2-x}O₄ and Li₂CrO₄ phases predicted by Raman spectroscopy, SEM-EDS, and XPS observations presented below are minor components of the oxide layer present on samples exposed to LiCl-Li₂O solutions in the absence of Li. Similar patterns were obtained for all samples exposed to LiCl-Li₂O

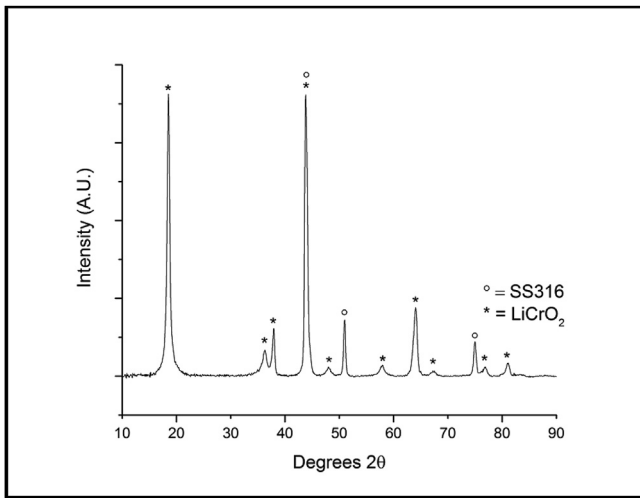


Fig. 9. GI-XRD pattern of SS316L exposed to LiCl-2%Li₂O-0%Li for 500hr after methanol rinsing. Peaks corresponding to LiCrO₂ and the base material were observed.

solutions in the absence of Li⁰.

The XRD patterns for SS316L samples exposed to LiCl-1wt%Li₂O solutions containing 0, 0.3, 0.6, or 1 wt%Li at 650 °C for 500hr are shown in Fig. 10, while Fig. 11 shows the diffraction patterns for SS316L samples exposed to identical conditions for 1000hr.

From these figures, it can be observed that the LiCrO₂ surface films that form in the absence of Li are not detectable via XRD in the presence of Li, corroborating SEM-EDS as well as the Raman spectroscopy and XPS analysis presented in this work [41]. These techniques all show that the presence of Li prevents the formation of appreciable oxide surface films, resulting in severe degradation to the base material. Additionally, de-austenization of the base material was observed on the SS316L samples exposed to LiCl-1wt%Li₂O containing 0, 0.6, and 1 wt%Li for 500hr, and LiCl-1wt%Li₂O containing 0 and 0.3 wt%Li for 1000hr. This effect was also observed in short term testing of SS316L in molten LiCl-Li₂O-Li [41]. The inconsistency with which this phenomena was observed indicates

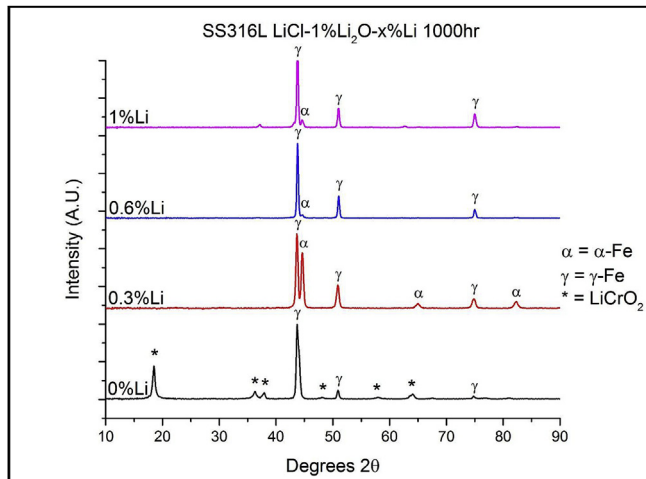


Fig. 11. High resolution grazing incidence XRD patterns for SS316L samples exposed to LiCl-1wt%Li₂O solutions containing 0, 0.3, 0.6, or 1 wt%Li at 650 °C for 1000hr. The diffraction pattern for the SS316L sample exposed to LiCl-1wt%Li₂O-0wt%Li shows the peaks identified as LiCrO₂ in Fig. 9, above. The extent of de-austenization of the base material varied among samples exposed to identical conditions, but otherwise the trends observed in Fig. 10 remain consistent at longer exposure periods.

that the solution chemistry does not affect the probability that a particular sample will undergo de-austenization. This is particularly highlighted by the SS316L samples exposed to LiCl-1wt%Li₂O containing 0.3, 0.6, and 1 wt%Li for 500 or 1000hr, as the samples exposed to identical solution chemistries for different exposure periods did not display similar de-austenization behavior.

The samples exposed to LiCl-2wt%Li₂O solutions containing 0, 0.3, 0.6, and 1 wt% Li displayed similar diffraction patterns as those presented here.

4.5. Raman Spectroscopy

The Raman spectrum of the SS316L sample exposed to LiCl-1wt%Li₂O-0wt%Li at 650 °C for 500hr is shown in Fig. 12. This spectrum displays peaks that were observed in various ratios on all samples exposed to LiCl-Li₂O solutions in the absence of Li and is therefore used here as representative of the samples exposed to similar

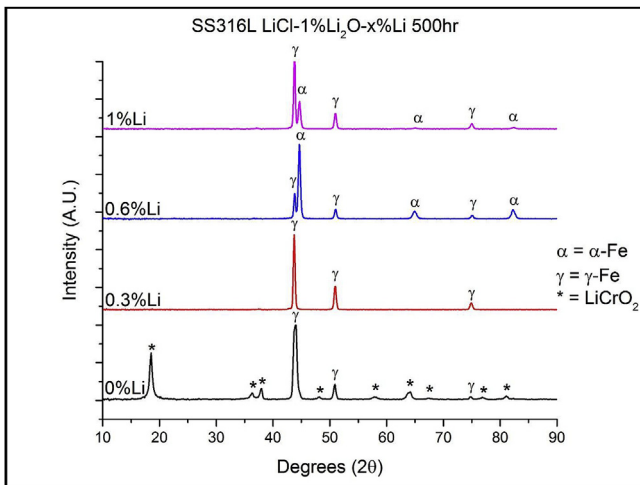


Fig. 10. High resolution grazing incidence XRD patterns for SS316L samples exposed to LiCl-1wt%Li₂O solutions containing 0, 0.3, 0.6, or 1 wt%Li at 650 °C for 500hr. The diffraction pattern for the SS316L sample exposed to LiCl-1wt%Li₂O-0wt%Li shows the peaks identified as LiCrO₂ in Fig. 10, above. The peaks of LiCrO₂ were not observed on any sample exposed to LiCl-Li₂O in the presence of Li. De-austenization of samples exposed to LiCl-1wt%Li₂O containing 0, 0.6, and 1 wt%Li for 500hr was observed.

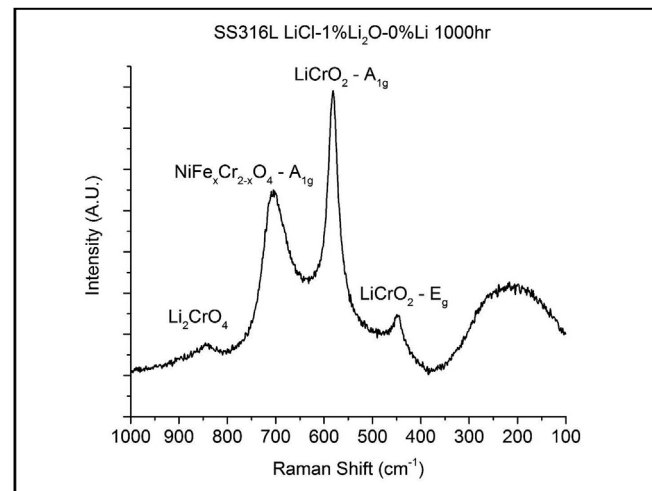


Fig. 12. Raman spectra of the SS316L sample exposed to LiCl-1wt%Li₂O in the absence of Li for 1000hr.

conditions. Both the A_{1g} mode at 572 cm^{-1} and the E_g mode at 445 cm^{-1} of LiCrO_2 are clearly defined [50]. Broad peaks centered at 250 cm^{-1} , 690 cm^{-1} , and 845 cm^{-1} were also observed. Based on EDS and XPS analysis shown in their respective sections, the peak at 690 cm^{-1} can be attributed to the A_{1g} mode of a mixed Ni, Fe, Cr spinel of the form $\text{NiFe}_x\text{Cr}_{2-x}\text{O}_4$, although the exact composition of this oxide is not easily identified [51]. The position of this peak was also observed to shift slightly on other samples, which can likely be attributed to variations in the stoichiometry of the spinel due to differing exposure periods, melt compositions, and base materials. The peak at 845 cm^{-1} is hypothesized to originate from Li_2CrO_4 , based on the presence of Cr^{6+} in the XPS spectra collected from SS316L samples exposed to $\text{LiCl}-\text{Li}_2\text{O}$ solutions in the absence of Li. The broad feature centered around 250 cm^{-1} could not be positively attributed to any single compound, but may be caused by the combination of the minor modes of Li_2CrO_4 and minor components of the $\text{NiFe}_x\text{Cr}_{2-x}\text{O}_4$ spectrum.

When exposed to $\text{LiCl}-\text{Li}_2\text{O}$ solutions containing Li, these oxide based surface films are destabilized due to the highly reducing nature of metallic Li. To illustrate the changes to the surface layer present on samples exposed to $\text{LiCl}-\text{Li}_2\text{O}$ solutions as a function of Li concentration, Fig. 13 shows the Raman spectra obtained from SS316L samples exposed to $\text{LiCl}-1\text{wt\%Li}_2\text{O}$ solutions containing 0, 0.3, 0.6, and 1 wt% Li at $650\text{ }^\circ\text{C}$ for 500 hr. The spectra collected from samples exposed to $\text{LiCl}-\text{Li}_2\text{O}$ in the presence of Li do not display any discernible features indicative of the well-developed oxide layer observed in Fig. 12. Rather, the features observed are broad and are close to the baseline of the instrument, indicating that the oxide layer is tenuously present on these samples.

As no investigations into the Raman spectra of Li_2CrO_4 could be found in literature, the spectra of a commercially purchased Li_2CrO_4 standard was collected to confirm that the peak seen at 845 cm^{-1} in Figs. 12 and 13 could be attributed to this compound. The Raman spectrum collected from pure Li_2CrO_4 is shown in Fig. 14. The assignment of specific vibrational and rotational modes to each of the peaks observed in Fig. 14 is beyond the scope of this study. However, it can be seen that the primary features of pure Li_2CrO_4 occur between 1000 cm^{-1} and 800 cm^{-1} , with the dominant peak occurring at approximately 850 cm^{-1} . Additional minor features are present between 450 cm^{-1} and 275 cm^{-1} . As the oxide layer of the samples is non-homogenous and consists primarily of LiCrO_2 with

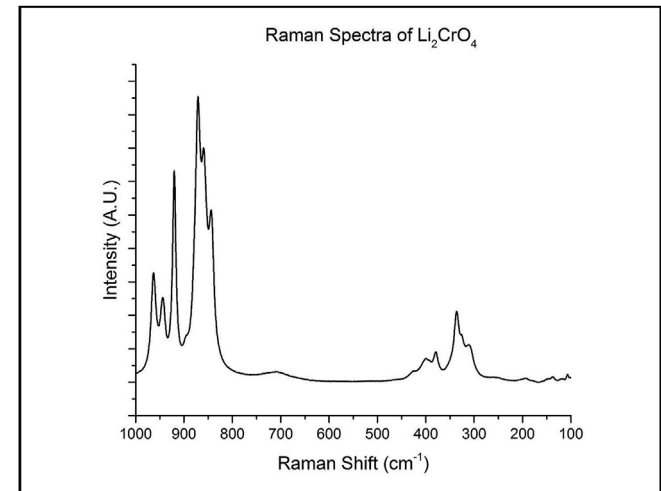


Fig. 14. Raman spectrum obtained from Li_2CrO_4 . Collection parameters were identical to those used for methanol rinsed samples. The primary features of the Li_2CrO_4 spectrum occur around 850 cm^{-1} , with minor features in the range of 450 cm^{-1} to 300 cm^{-1} .

small amounts of $\text{NiFe}_x\text{Cr}_{2-x}\text{O}_4$ and Li_2CrO_4 , the smearing of the features of the Li_2CrO_4 spectrum to form the single, broad peak centered around 850 cm^{-1} observed on the samples exposed to $\text{LiCl}-\text{Li}_2\text{O}$ is plausible [51].

4.6. X-ray photoelectron spectroscopy

XPS survey scans of the SS316L samples exposed to $\text{LiCl}-1\text{wt\%Li}_2\text{O}$ containing 0, 0.3, 0.6, and 1 wt% Li at $650\text{ }^\circ\text{C}$ for 1000 hr are shown in Fig. 15. For the SS316L sample exposed to $\text{LiCl}-1\text{wt\%Li}_2\text{O}$ at $650\text{ }^\circ\text{C}$ for 1000 hr in the absence of Li, the surface is primarily composed of Cr and O, with Ni and Fe detectable in small quantities. For the SS316L samples exposed to $\text{LiCl}-1\text{wt\%Li}_2\text{O}$ containing 0.6 and 1 wt% Li at $650\text{ }^\circ\text{C}$ for 1000 hr, the surface shows a relatively thick Ti-based surface deposit, with high quantities of N and O present. In the case of the SS316L sample exposed to $\text{LiCl}-1\text{wt\%Li}_2\text{O}-0.6\text{ wt\%Li}$ for 1000 hr, this Ti surface film was sufficiently thick to prevent the analysis of the underlying base material. TiO_2 is a common impurity in Li_2O , and the deposition of Ti based

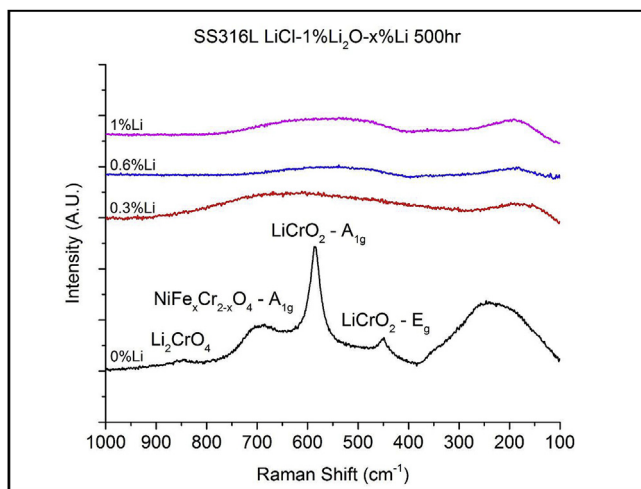


Fig. 13. Raman spectra of SS316L samples exposed to molten $\text{LiCl}-1\text{wt\%Li}_2\text{O}$ containing 0, 0.3, 0.6, and 1 wt% Li for 500 h. The distinctive peaks characteristic of LiCrO_2 , Li_2CrO_4 and $\text{NiFe}_x\text{Cr}_{2-x}\text{O}_4$ observed on samples exposed to $\text{LiCl}-\text{Li}_2\text{O}$ in the absence of Li are seen to be eliminated by the presence of Li in the melt.

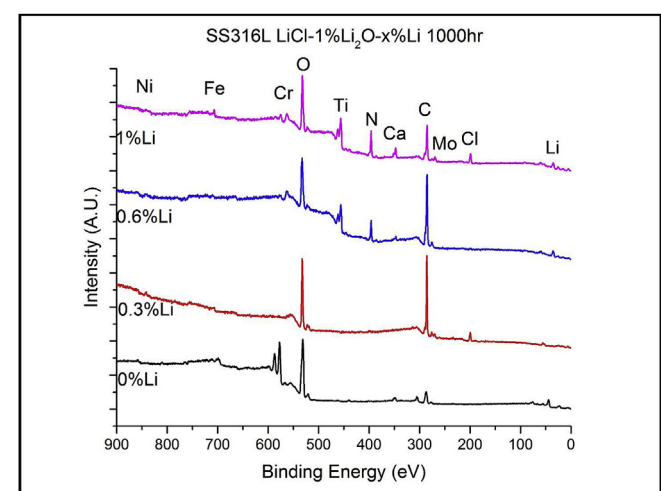


Fig. 15. XPS survey spectra recorded on SS316L samples exposed to $\text{LiCl}-1\text{wt\%Li}_2\text{O}$ containing 0, 0.3, 0.6, and 1 wt% Li at $650\text{ }^\circ\text{C}$ for 1000 hr after rinsing in methanol.

compounds on samples exposed to LiCl-Li₂O in the presence of Li was extensively studied during our previous short term studies [48].

Analysis of the alloying elements, especially the Cr 2p spectra, is necessary to determine the corrosion mechanisms of SS316L in LiCl-Li₂O-Li, as Cr is the primary element responsible for the formation of oxide films in the absence of Li. Identification of the oxidation state of Cr present on the surface of the SS316L sample exposed to LiCl-1wt%Li₂O-Li at 650 °C for 500hr was performed by peak fitting the Cr 2p_{3/2} spectra using previously published peak fitting parameters [52]. The peak fit data for all Cr spectra collected on the samples in this study are shown in Fig. 16, while the peak fitting parameters are given in Table 6 [52].

As can be observed in Fig. 16, both Cr³⁺ and Cr⁶⁺ are simultaneously present on all SS316L samples exposed to LiCl-Li₂O solutions in the absence of Li⁰. The presence of Cr³⁺ and Cr⁶⁺ on the samples further supports the presence of both LiCrO₂ (Cr³⁺) and Li₂CrO₄ (Cr⁶⁺) on the surfaces of samples exposed to LiCl-Li₂O solutions in the absence of Li. In the presence of Li, the highly reducing nature of metallic Li destabilizes the oxide films that are present on the sample surfaces in the absence of Li. However, the transition between electrochemical oxidation of the samples in the absence of Li and liquid metal attack in the presence of high Li

concentrations is not abrupt. Our previous short term studies have shown that at concentrations at or below the apparent solubility limit of Li in the system (around 0.3 wt%Li) [24], there exists a transition region where both modes of attack occur simultaneously [41,42]. The Cr 2p_{3/2} spectra shown in Fig. 16 give further evidence for this hypothesis, although there was no discernible trend in the relative ratios of Cr⁰, Cr³⁺, and Cr⁶⁺ based on the concentration of Li, Li₂O, or exposure period.

The presence of Cr³⁺ is also required for the formation of NiFe_xCr_{2-x}O₄, as both Fe and Cr are in the 3+ oxidation state in this compound, while Ni is present in the 2+ oxidation state. Further confirmation of the presence of NiFe_xCr_{2-x}O₄ is given by the narrow scans of the Ni 2p and Fe 2p spectra for SS316L exposed to LiCl-1wt%Li₂O-0wt%Li for 500hr, which are shown in Fig. 17, along with the Ni 2p and Fe 2p narrow scans for the SS316L sample exposed to LiCl-1wt%Li₂O-0.3 wt%Li for 500hr. In the absence of Li, the Ni 2p_{3/2} peak is located at 853.5eV, while the Fe 2p_{3/2} peak is located at 710.1eV. These binding energies and peak shapes correspond to Ni²⁺ and Fe³⁺, respectively [53]. Neither element was detected in the metallic state, confirming the presence of Ni and Fe based oxides on the sample surface. In conjunction with Raman spectroscopy and EDS analysis, this is further evidence supporting the presence of a NiFe_xCr_{2-x}O₄ based spinel present on the surface of

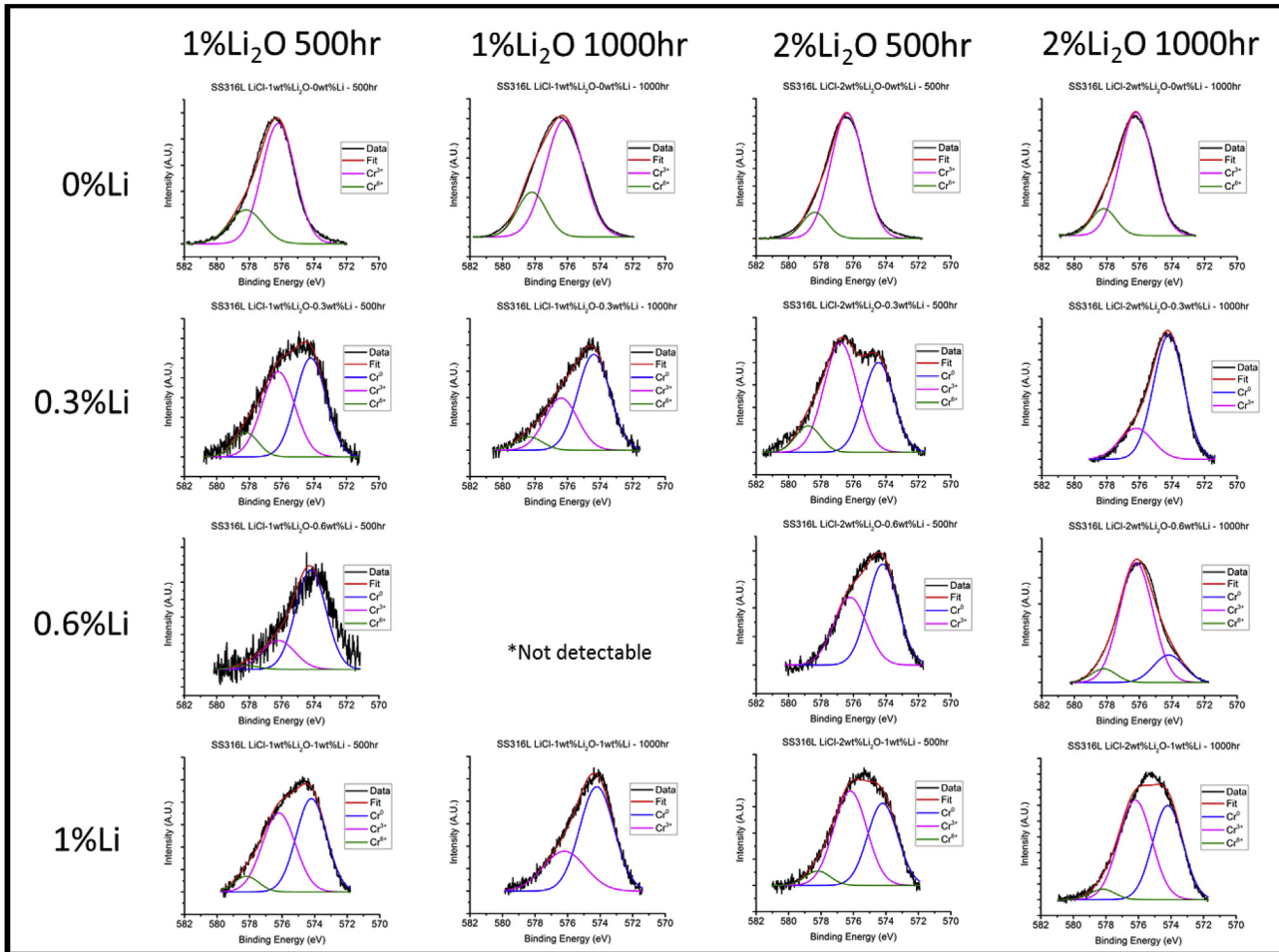


Fig. 16. Cr 2p XPS spectra collected from SS316L samples exposed to all LiCl-Li₂O-Li compositions and exposure periods studied in this work. Charge correction was performed to the adventitious C 1s peak at 284.8eV, and peak fitting parameters for Cr⁰, Cr³⁺, and Cr⁶⁺ listed in Table 2 were used for all spectra. Cr³⁺ and Cr⁶⁺ are the only species present in the absence of Li. Cr spectra of SS316L samples exposed to molten LiCl-Li₂O in the presence of Li indicate both metallic and oxidized components; however, no discernible trend in oxidation state based on Li concentration, Li₂O concentration or exposure period could be determined. Cr was not detectable on the SS316L sample exposed to LiCl-1wt% Li₂O-0.6 wt% Li for 1000hr due to the thickness of the overlying Tl surface deposit.

Table 6

Peak fitting parameters used for Cr 2p_{3/2} spectra reported in Fig. 9 [52].

Peak	BE	FWHM
Cr ⁰	574.2	2.2
Cr ³⁺	576.2	2.4
Cr ⁶⁺	578.2	1.8

the samples exposed to LiCl-Li₂O in the absence of Li. However, when Li was present in the molten salt, only metallically bonded Ni and Fe are present on the sample surface. No charge correction was necessary for the Ni and Fe 2p spectra, indicating that these elements were in direct electrical contact with the base material. Similar spectra were recorded for all other SS316L samples exposed to LiCl-Li₂O-Li, indicating that any quantity of Li⁰ in the melt is sufficient to reduce NiFe_xCr_{2-x}O₄.

In our previous work, Mo was observed to behave similarly to Cr in some respects, becoming enriched on the surface in the absence of Li, and depleted at higher Li concentrations. As Mo is a minor alloying element of SS316L at around 2 wt%, Mo was not observed on all samples. Additionally, in the absence of Li, Mo was not detectable via XPS on any sample due to the thick LiCrO₂ surface layer. However, the samples exposed to molten LiCl-2wt%Li₂O solutions containing 0.3, 0.6, and 1 wt%Li for 500hr all had detectable levels of Mo, the narrow scans of which are presented in Fig. 18. From the spectra in Fig. 18, it can be observed that when 0.3 wt% Li is present in solution, Mo⁶⁺ is the only Mo species observable on the sample surface [54]. However, as Li concentration increases the

stability of oxidized Mo is decreased, resulting in a mixed Mo⁶⁺/Mo⁰ spectra at 0.6 wt% Li and a fully metallic Mo⁰ spectra at 1 wt% Li [54,55]. The observation of Mo⁶⁺ on samples exposed to high concentrations of Li indicates that Mo is highly active in the LiCl-Li₂O-Li system, which could explain the depletion of Mo from the surface of SS316L observed via SEM-EDS analysis of the cross section of these samples in section 4.2.

Co was also observed on some samples exposed to LiCl-Li₂O in the presence of Li. Co is not an alloying element of SS316L, but is present as the primary impurity in the Ni crucibles used for these studies at concentrations of less than 1 wt%. Consequently, the presence of Co on the surface of the samples exposed to LiCl-Li₂O solutions in the presence of Li indicates that there is mass transport from the crucible to the samples. Mass transport of Co from the crucible to the samples had not been observed in our previous short term experiments [41,42,44]. The Co 2p spectra of the SS316L sample exposed to LiCl-1wt%Li₂O-0.3 wt%Li for 500hr is presented in Fig. 19, and is typical of Co³⁺, due to its binding energy and peak shape [53]. The cause of the transport of Co from the crucible to the samples and its implications to the degradation of materials in the LiCl-Li₂O-Li system as a whole requires further investigation.

5. Conclusions

Exposure testing of SS316L samples was performed for 500 and 1000hr intervals in molten LiCl-Li₂O-Li solutions containing 1 and 2 wt% Li₂O and 0, 0.3, 0.6, and 1 wt% Li. Morphological and elemental changes to the sample surfaces and cross sections were

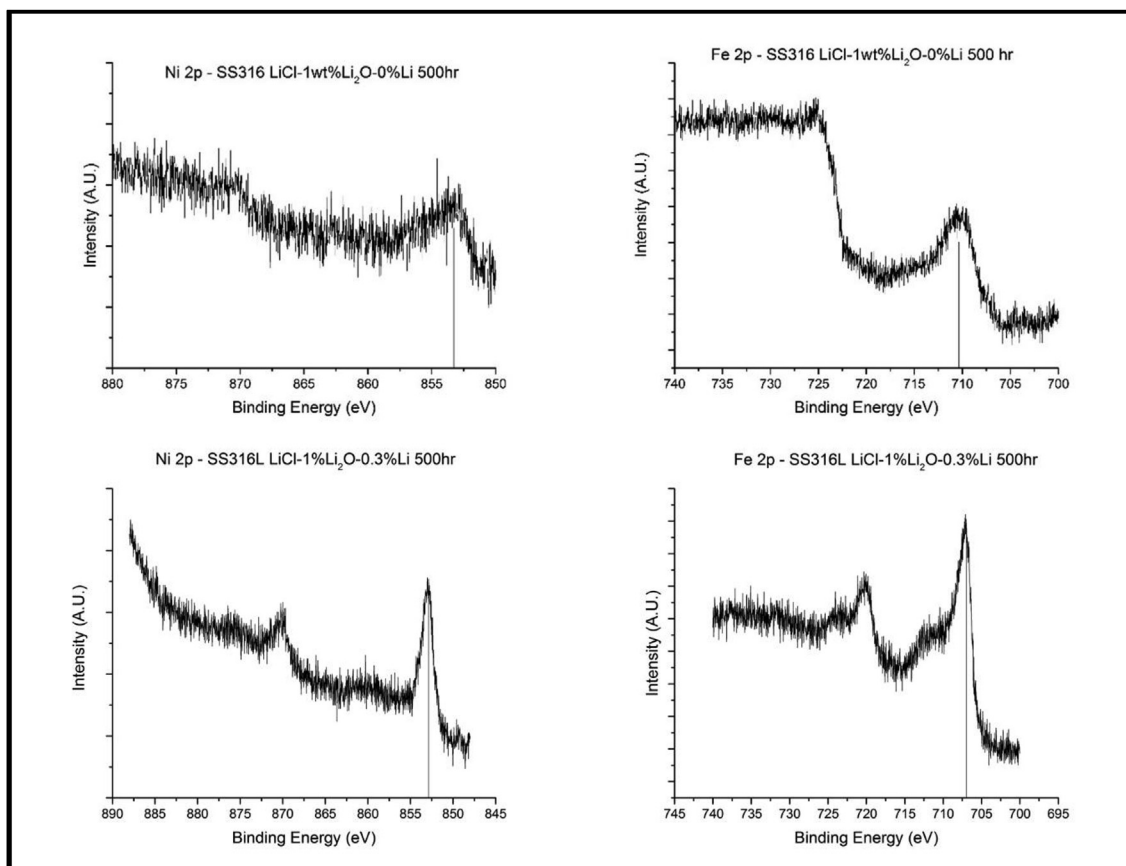


Fig. 17. XPS narrow scans for Ni 2p (left) and Fe 2p (right) collected from SS316L exposed to LiCl-1%Li₂O-0%Li (Top) and LiCl-1wt%Li₂O-0.3 wt%Li (Bottom) at 650 °C for 500hr. In the absence of Li, Ni is present in the 2+ oxidation state and Fe is present in the 3+ oxidation state based on their binding energies of 853.5eV and 710.1eV, respectively. However, in the presence of Li, all Ni and Fe spectra indicate the presence only of metallic Ni and Fe.

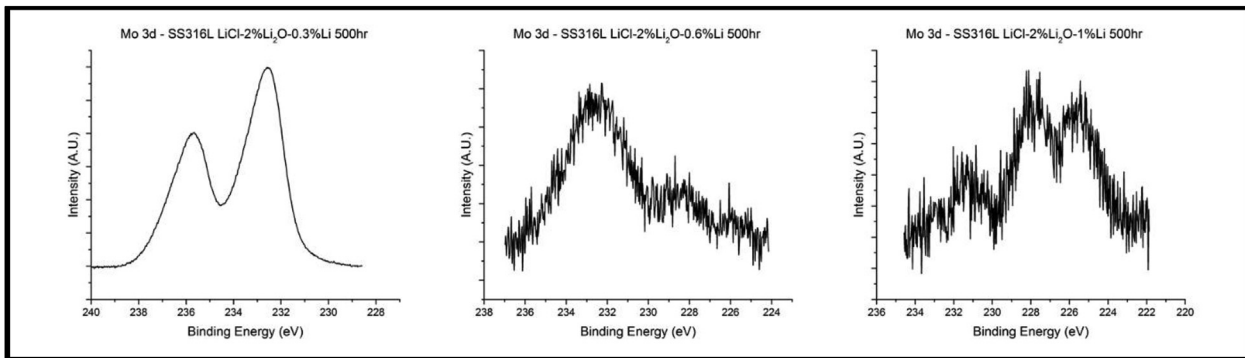


Fig. 18. Mo 3d XPS spectra of SS316L samples exposed to molten LiCl-2wt%Li₂O solutions containing 0.3, 0.6, and 1 wt%Li for 500hr. As Li concentration in the melt is increased, the Mo oxidation state shifts towards more reduced species. The peak shape for the SS316L sample exposed to LiCl-2wt%Li₂O-1wt%Li for 500hr is likely the result of differential charging and the charge correction performed to the adventitious C 1S peak at 284.8eV.

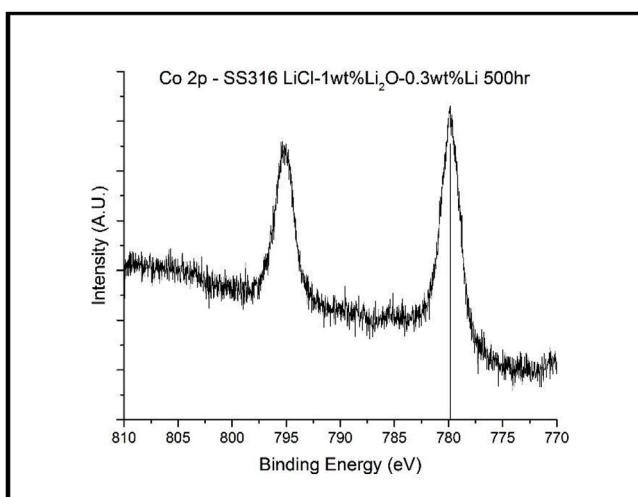


Fig. 19. XPS narrow scan of the Co 2p peak observed on SS316L exposed to LiCl-1wt%Li₂O-0.3wt%Li at 650 °C for 500hr and rinsed with methanol. The binding energy and shape of the 2p_{3/2} peak of 789.8eV is consistent with the presence of Co³⁺ [56].

investigated via SEM and EDS, respectively, while XRD, Raman spectroscopy, and XPS were used to provide further insight into the effect of Li⁰ on the degradation mechanisms of materials in LiCl-Li₂O-Li. Upon exposure to LiCl-Li₂O solutions in the absence of Li, SS316L was observed to form a LiCrO₂ based surface film, with minor contributions of Li₂CrO₄ and NiFe_xCr_{2-x}O₄. The oxide layer limited corrosion to a rate of approximately 0.24 mm/year during exposure to molten LiCl-Li₂O solutions. The presence of Li in the melt resulted in the destabilization of the protective oxide film formed in LiCl-Li₂O solutions, causing substantial damage to the samples in the form of intergranular corrosion. XPS analysis observed that metallically bonded Ni and Fe were present on the surface of all SS316L samples exposed to LiCl-Li₂O in the presence of Li, however both Cr and Mo displayed varying degrees of oxidation in the presence of Li. Mass loss rates were low, but cross sectioned samples displayed significant ingress of LiCl and damage to the sample surface, indicating that mass loss measurements alone are not sufficient to characterize corrosion in this system. Intergranular corrosion was facilitated by the precipitation of metal carbides and nitrides along the grain boundaries, resulting in the selective depletion of alloying elements, such as Cr, Mo, and Mn. The rate of material damage was on the order of 2–3 mm/year, indicating that the presence of high concentrations of Li during the electrolytic

reduction of UNF will dramatically reduce the lifetime of any SS316L components exposed to the electrolyte. The ingress of intergranular corrosion into the material will likely have a marked effect on the strength of the material due to the effective loss of structural thickness, however, further investigation would be necessary to validate this hypothesis. From the combination of analytical techniques presented in this work, it is hypothesized that cyclical oxidation by O²⁻ ions and reduction by Li⁰ is responsible for the high levels of material degradation in the LiCl-Li₂O-Li system.

Data availability

The raw/processed data required to reproduce these findings cannot be shared at this time as the data also forms part of an ongoing study.

Acknowledgements

The authors gratefully thank Zachary Karmiol, Research Scientist at Materials Characterization Nevada, for analyses of the cross sectioned samples.

This work was performed under the auspices of the Department of Energy (DOE), United States under contracts DE-NE0008262 and DE-NE0008236, and the US Nuclear Regulatory Commission (USNRC), United States under contracts NRCHQ-11-G-38-0039 and NRC-HQ-13-G-38-0027. W.P. acknowledges the Fellowship Award from the USNRC. Dr. Kenny Osborne serves as the program manager for the DOE award and Ms. Nancy Hebron-Isreal serves as the grants program officer for the NRC awards.

Appendix A. Supplementary data

Supplementary data to this article can be found online at <https://doi.org/10.1016/j.jnucmat.2019.02.007>.

References

- [1] K. Gourishankar, L. Redey, M. Williamson, Electrolytic reduction of metal oxides in molten salts, in: W.A. Schneider (Ed.), Light Metals, the Minerals, Metals & Materials Society, 2002.
- [2] S.D. Herrmann, S.X. Li, M.F. Simpson, Electrolytic Reduction of Spent Oxide Fuel - Bench-Scale Test Results, GLOBAL 2005, Tsukuba, Japan, 2005.
- [3] H. Lee, G.-I. Park, K.-H. Kang, J.-M. Hur, J.-G. Kim, D.-H. Ahn, Y.-Z. Cho, E.H. Kim, Nucl. Eng. Technol. 43 (2011) 317–328.
- [4] M. Kurata, T. Inoue, J. Serp, M. Ougier, J.P. Glatz, J. Nucl. Mater. 328 (2004) 97–102.
- [5] S.D. Herrmann, S.X. Li, M.F. Simpson, S. Phongikaroon, Separ. Sci. Technol. 41 (2006) 1965–1983.
- [6] M. Iizuka, Y. Sakamura, T. Inoue, J. Nucl. Mater. 359 (2006) 102–113.
- [7] B. Park, S. Park, S. Jeong, C. Seo, J. Radioanal. Nucl. Chem. 270 (2006) 575–583.

- [8] C.S. Seo, S.B. Park, B.H. Park, K.J. Jung, S.W. Park, S.H. Kim, J. Nucl. Sci. Technol. 43 (2006) 587–595.
- [9] S. Jeong, J. Hur, S. Hong, D. Kang, M. Choung, X. Seo, J. Yoon, S. Park, Nucl. Technol. 162 (2007) 184–191.
- [10] B.H. Park, I.W. Lee, C.S. Seo, Chem. Eng. Sci. 63 (2008) 3485–3492.
- [11] S. Herrmann, S. Li, B. Serrano-Rodriguez, Observations of Oxygen Ion Behavior in the Lithium-Based Electrolytic Reduction of Uranium Oxide, GLOBAL 2009, Idaho National Labs, Paris, France, 2009, pp. 1198–1206.
- [12] S. Herrmann, S. Li, D. Sell, B. Westphal, Electrolytic Reduction of Spent Nuclear Oxide Fuel – Effects of Fuel Form and Cathode Containment Materials on Bench-Scale Operations, Idaho National Laboratory, 2007.
- [13] S.X. Li, M.F. Simpson, S.D. Hermann, Oxygen ion oxidation process on a platinum electrode in LiCl-Li₂O at 650°C, in: R.A. Mantz (Ed.), Electrochemical Society Proceedings, vol. 24, 2004.
- [14] A. Merwin, D. Chidambaram, Metall. Mater. Trans. 46 (2015) 536–544.
- [15] T. Usami, T. Kato, M. Kurata, T. Inoue, H.E. Sims, S.A. Beetham, J.A. Jenkins, J. Nucl. Mater. 304 (2002) 50–55.
- [16] A. Merwin, M.A. Williamson, J.L. Willit, D. Chidambaram, J. Electrochem. Soc. 164 (2017) H5236–H5246.
- [17] W. Park, J.-M. Hur, S.-S. Hong, E.-Y. Choi, H.S. Im, S.-C. Oh, J.-W. Lee, J. Nucl. Mater. 441 (2013) 232–239.
- [18] A.S. Dworkin, H.R. Bronstein, M.A. Bredig, J. Phys. Chem. 66 (1962) 572–573.
- [19] T. Nakajima, R. Minami, K. Nakanishi, N. Watanabe, Bull. Chem. Soc. Jpn. 47 (1974) 2071–2072.
- [20] T. Nakajima, K. Nakanishi, N. Watanabe, Nippon Kagaku Kaishi 1975 (1975) 617–621.
- [21] T. Nakajima, K. Nakanishi, N. Watanabe, Bull. Chem. Soc. Jpn. 49 (1975) 994–997.
- [22] J. Liu, J.C. Poignet, J. Appl. Electrochem. 20 (1990) 864–867.
- [23] T. Usami, M. Kurata, T. Inoue, H.E. Sims, S.A. Beetham, J.A. Jenkins, J. Nucl. Mater. 300 (2002) 15–26.
- [24] T.N. Nakajima, N. Watanabe, Nippon Kagaku Kaishi 1974 (1974) 401–404.
- [25] M.A. Bredig, in: M. Blander (Ed.), Molten Salt Chemistry, John Wiley and Sons, 1964, pp. 367–425, 1964.
- [26] A. Merwin, W.C. Phillips, M.A. Williamson, J.L. Willit, P.N. Motsegood, D. Chidambaram, Sci. Rep. 6 (2016) 25435.
- [27] S.H. Cho, J.S. Zhang, Y.J. Shin, S.W. Park, H.S. Park, J. Nucl. Mater. 325 (2004) 13–17.
- [28] R.Y. Liu, X. Wang, J.S. Zhang, X.M. Wang, J. Nucl. Mater. 327 (2004) 194–201.
- [29] C. Soo-Haeng, L. Jong-Ho, P. Sung-Bin, J. Ki-Jung, P. Seong-Won, J. Kor. Inst. Met. Mater. 43 (2005) 449–454.
- [30] Q. Gao, R.Y. Liu, J.S. Zhang, J.T. Guo, Mater. Lett. 59 (2005) 2052–2058.
- [31] S.H. Cho, S.B. Park, J.H. Lee, J.M. Hur, H.S. Lee, Mater. Chem. Phys. 131 (2012) 743–751.
- [32] C. Soo-Haeng, P. Seong-Bin, L. Jong-Hyeon, H. Jin-Mok, L. Han-Soo, Oxid. Metals 78 (2012) 153–165.
- [33] P. SangKyu, L. Taehyuk, S. MoonSoo, N. JaeSoo, C. SooHaeng, L. JongHyeon, Adv. Mater. Res. 886 (2014) 41–44.
- [34] H.-Y. Lee, K.-H. Baik, Met. Mater. Int. 15 (2009) 783–787.
- [35] T.R. Allen, K. Sridharan, Corrosion in molten salts, in: Molten Salts Chemistry from Lab to Applications, Elsevier, Burlington, MA, 2013.
- [36] Y.S. Zhang, J. Electrochem. Soc. 133 (1986) 655.
- [37] J.E. Indacochea, J.L. Smith, K.R. Litko, E.J. Karel, J. Mater. Res. 14 (1999) 1990–1995. M1993 - 1910.1557/JMR.1999.0268.
- [38] J.E. Indacochea, J.L. Smith, K.R. Litko, E.J. Karel, A.G. Raraz, Oxid. Metals 55 (1999) 1–16.
- [39] B. Mishra, D.L. Olson, Miner. Process. Extr. Metall. Rev. 22 (2001) 369–388.
- [40] S.H. Cho, S.B. Park, J.H. Lee, J.M. Hur, H.S. Lee, J. Nucl. Mater. 412 (2011) 157–164.
- [41] A. Merwin, D. Chidambaram, Corros. Sci. 126 (2016) 1–9.
- [42] A. Merwin, D. Chidambaram, Nucl. Technol. 195 (2016) 204–212.
- [43] E.-Y. Choi, J. Lee, J. Nucl. Mater. 495 (2017) 85–90.
- [44] W. Phillips, A. Merwin, D. Chidambaram, Metall. Mater. Trans. 49 (2018) 2384–2392.
- [45] N.J. Gese, The Electrochemistry of Li-LiCl-Li₂O Molten Salt Systems and the Role of Moisture, Nuclear Engineering, University of Idaho, 2015.
- [46] D.A. Jones, Principles and Prevention of Corrosion, Prentice Hall, Upper Saddle River, NJ, 1996.
- [47] J.E. Indacochea, J.L. Smith, K.R. Litko, E.J. Karel, A.G. Rarez, Oxid. Metals 55 (2001) 1–16.
- [48] A. Merwin, Material Interactions with Molten LiCl-Li₂O-Li, Materials Science and Engineering, Vol Doctor of Philosophy in Materials Science and Engineering, University of Nevada, Reno, 2016, p. 241.
- [49] PDF Card No. : 01-072-7839, The International Centre for Diffraction Data.
- [50] M. Suzuki, I. Yamada, H. Kadowaki, F. Takei, J. Phys. Condens. Matter 5 (1993) 4225–4232.
- [51] B.D. Hosterman, Raman Spectroscopic Study of Solid Solution Spinel Oxides, Physics and Astronomy, Vol Doctor of Philosophy in Physics, UNLV, 2011, p. 155.
- [52] D. Chidambaram, C.R. Clayton, G.P. Halada, J. Electrochem. Soc. 150 (2003) B224–B237.
- [53] M.C. Biesinger, B.P. Payne, A.P. Grosvenor, L.W.M. Lau, A.R. Gerson, R.S.C. Smart, Appl. Surf. Sci. 257 (2011) 2717–2730.
- [54] B. Brox, I. Olefjord, Surf. Interface Anal. 13 (1988) 3–6.
- [55] J. Baltrusaitis, B. Mendoza-Sanchez, V. Fernandez, R. Veenstra, N. Dukstiene, A. Roberts, N. Fairley, Appl. Surf. Sci. 326 (2015) 151–161.
- [56] M.C. Biesinger, B.P. Payne, A.P. Grosvenor, L.W.M. Lau, A.R. Gerson, R.S.C. Smart, Appl. Surf. Sci. 257 (2011) 2717–2730.